Electronic Supplementary Material (ESI) for New Journal of Chemistry.

Both magnetic relaxation and luminescence of Zn_2Dy_2 cluster complexes regulated by the bis-imine chain in Schiff base ligands

Cai-Ming Liu,[†*] De-Qing Zhang,[†] Yi-Quan Zhang,[*,‡] Miao Li,[‡] and Dao-Ben Zhu[†]

[†]*Beijing National Laboratory for Molecular Sciences, Center for Molecular Science, Key Laboratory of Organic Solids, Institute of Chemistry, CAS Research/Education Center for Excellence in Molecular Science, Chinese Academy of Sciences, Beijing 100190, China.*

[‡]*Jiangsu Key Laboratory for NSLSCS, School of Physical Science and Technology, Nanjing Normal University, Nanjing, 210023, China.*

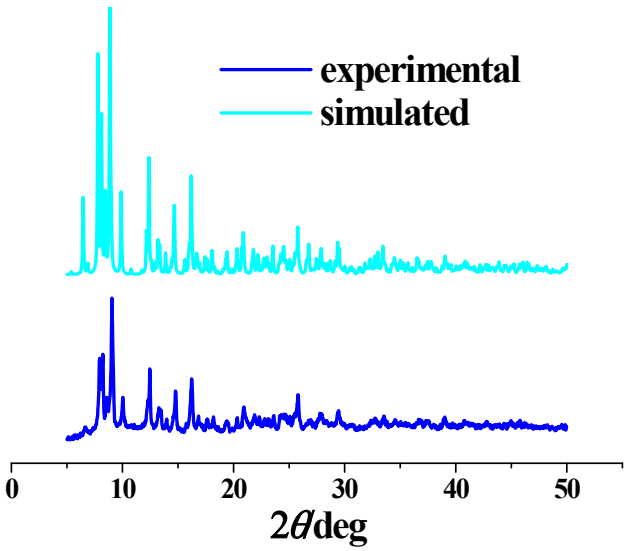

Fig. S1. The simulative and experimental powder X-ray diffraction patterns for **1**.

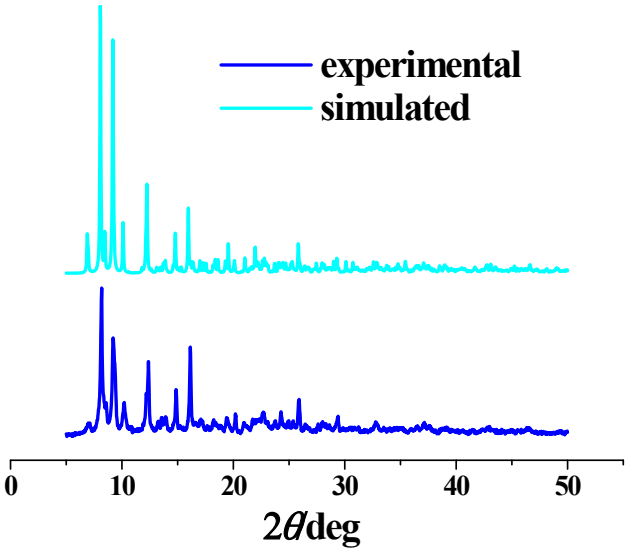

Fig. S2. The simulative and experimental powder X-ray diffraction patterns for **2**.

Table S1. Continuous Shape Measures calculation for Dy1 atom in **1**.

Dy1 structure

EP-9	1 D9h	Enneagon
OPY-9	2 C8v	Octagonal pyramid
HBPY-9	3 D7h	Heptagonal bipyramid
JTC-9	4 C3v	Johnson triangular cupola J3
JCCU-9	5 C4v	Capped cube J8
CCU-9	6 C4v	Spherical-relaxed capped cube
JCSAPR-9	7 C4v	Capped square antiprism J10
CSAPR-9	8 C4v	Spherical capped square antiprism
JTCTPR-9	9 D3h	Tricapped trigonal prism J51
TCTPR-9	10 D3h	Spherical tricapped trigonal prism
JTDIC-9	11 C3v	Tridiminished icosahedron J63
HH-9	12 C2v	Hula-hoop
MFF-9	13 Cs	Muffin

Structure [ML9]	EP-9	OPY-9	HBPY-9	JTC-9	JCCU-9	CCU-9	JCSAPR-9	CSAPR-9	JTCTPR-9	TCTPR-9	JTDIC-9	HH-9	**MFF-9**
ABOXIY,	34.294,	21.784,	17.181,	14.367,	7.265,	6.387,	3.750,	2.454,	4.595,	3.448,	11.576,	6.761,	**2.257**

Table S2. Continuous Shape Measures calculation for Dy2 atom in **1**.

Dy2 structure

OP-8	1 D8h	Octagon
HPY-8	2 C7v	Heptagonal pyramid
HBPY-8	3 D6h	Hexagonal bipyramid
CU-8	4 Oh	Cube
SAPR-8	5 D4d	Square antiprism
TDD-8	6 D2d	Triangular dodecahedron
JGBF-8	7 D2d	Johnson gyrobifastigium J26
JETBPY-8	8 D3h	Johnson elongated triangular bipyramid J14
JBTPR-8	9 C2v	Biaugmented trigonal prism J50
BTPR-8	10 C2v	Biaugmented trigonal prism
JSD-8	11 D2d	Snub diphenoid J84
TT-8	12 Td	Triakis tetrahedron
ETBPY-8	13 D3h	Elongated trigonal bipyramid

Structure [ML8]	OP-8	HPY-8	HBPY-8	CU-8	SAPR-8	TDD-8	JGBF-8	JETBPY-8	JBTPR-8	BTPR-8	**JSD-8**	TT-8	ETBPY-8
ABOXIY,	31.758,	26.314,	13.193,	11.548,	4.793,	2.632,	9.335,	25.139,	3.698,	3.452,	**2.618**,	12.319,	21.496

Table S3. Continuous Shape Measures calculation for Dy1 atom in **2**.

Dy1 structure

EP-9	1 D9h	Enneagon
OPY-9	2 C8v	Octagonal pyramid
HBPY-9	3 D7h	Heptagonal bipyramid
JTC-9	4 C3v	Johnson triangular cupola J3
JCCU-9	5 C4v	Capped cube J8
CCU-9	6 C4v	Spherical-relaxed capped cube
JCSAPR-9	7 C4v	Capped square antiprism J10
CSAPR-9	8 C4v	Spherical capped square antiprism
JTCTPR-9	9 D3h	Tricapped trigonal prism J51
TCTPR-9	10 D3h	Spherical tricapped trigonal prism
JTDIC-9	11 C3v	Tridiminished icosahedron J63
HH-9	12 C2v	Hula-hoop
MFF-9	13 Cs	Muffin

Structure [ML9]	EP-9	OPY-9	HBPY-9	JTC-9	JCCU-9	CCU-9	JCSAPR-9	CSAPR-9	JTCTPR-9	TCTPR-9	JTDIC-9	HH-9	**MFF-9**
ABOXIY,	34.056,	21.742,	17.667,	14.731,	7.411,	6.714,	4.392,	2.989,	5.183,	3.808,	11.241,	6.640,	**2.832**

Table S4. Continuous Shape Measures calculation for Dy2 atom in **2**.

Dy2 structures

OP-8	1 D8h	Octagon
HPY-8	2 C7v	Heptagonal pyramid
HBPY-8	3 D6h	Hexagonal bipyramid
CU-8	4 Oh	Cube
SAPR-8	5 D4d	Square antiprism
TDD-8	6 D2d	Triangular dodecahedron
JGBF-8	7 D2d	Johnson gyrobifastigium J26
JETBPY-8	8 D3h	Johnson elongated triangular bipyramid J14
JBTPR-8	9 C2v	Biaugmented trigonal prism J50
BTPR-8	10 C2v	Biaugmented trigonal prism
JSD-8	11 D2d	Snub diphenoid J84
TT-8	12 Td	Triakis tetrahedron
ETBPY-8	13 D3h	Elongated trigonal bipyramid

Structure [ML8]	OP-8	HPY-8	HBPY-8	CU-8	SAPR-8	TDD-8	JGBF-8	JETBPY-8	JBTPR-8	**BTPR-8**	JSD-8	TT-8	ETBPY-8
ABOXIY,	33.066,	25.974,	13.060,	11.125,	4.955,	2.763,	9.094,	24.732,	3.977,	3.783,	**2.616**,	11.836,	21.079

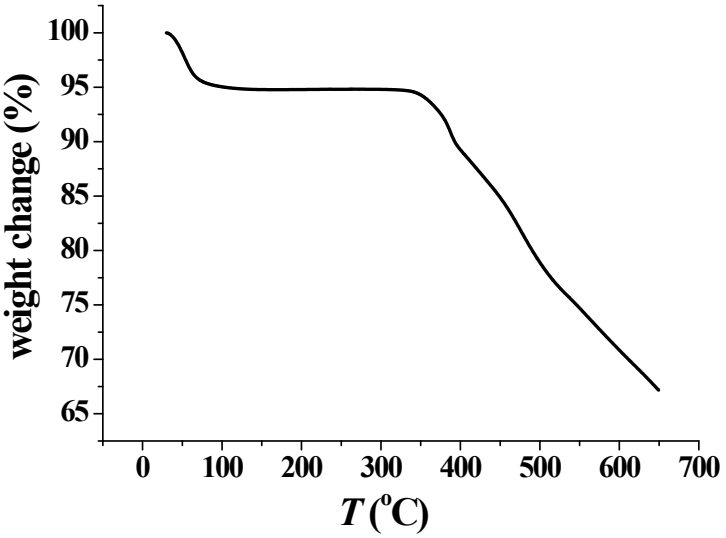

Fig. S3. TGA curve for **1**.

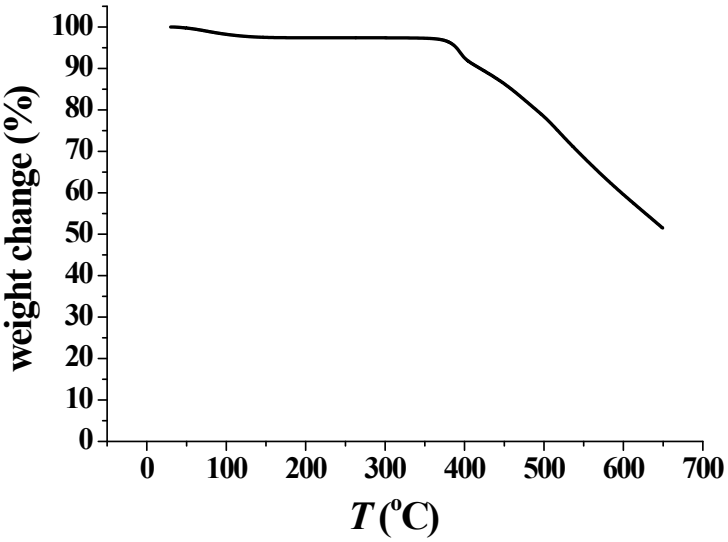

Fig. S4. TGA curve for **2**.

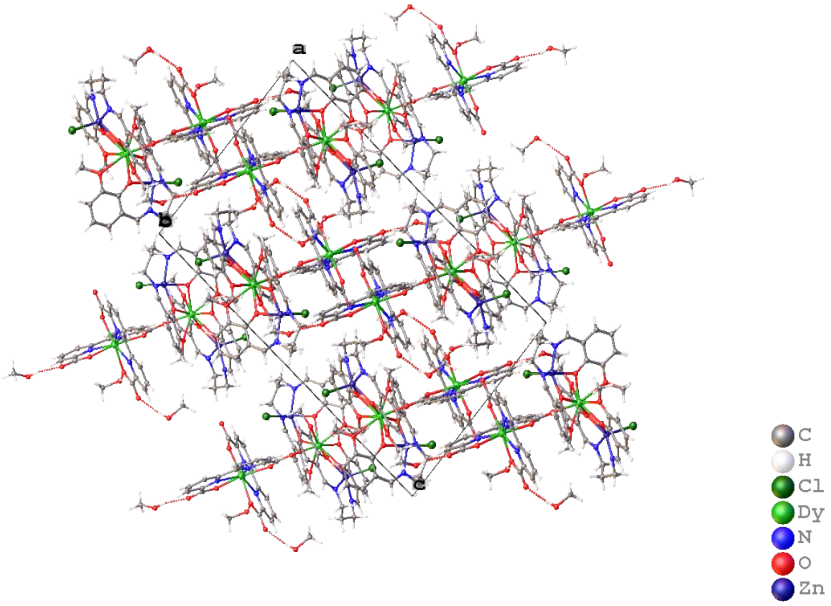

Fig. S5. Unit cell packing diagram of **1**.

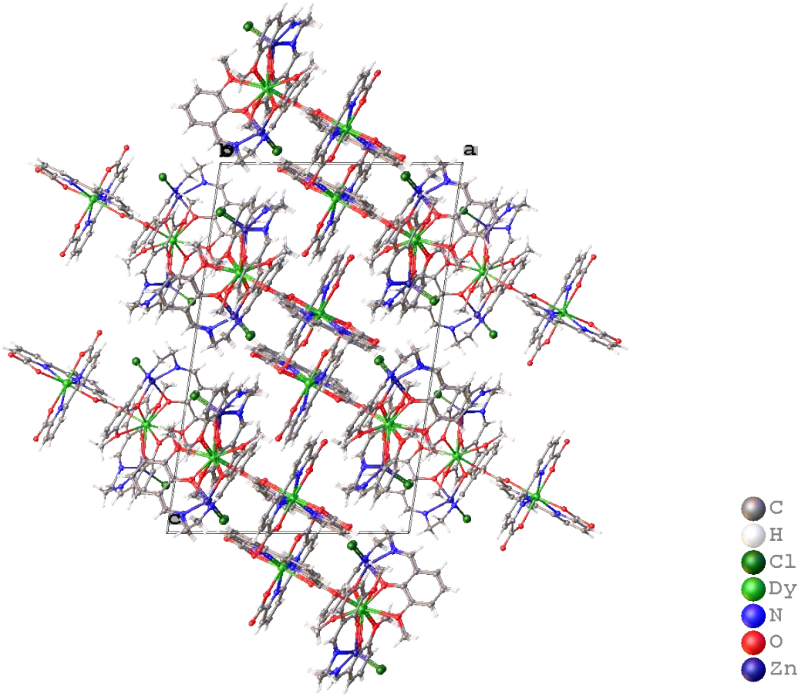

Fig. S6. Unit cell packing diagram of **2**.

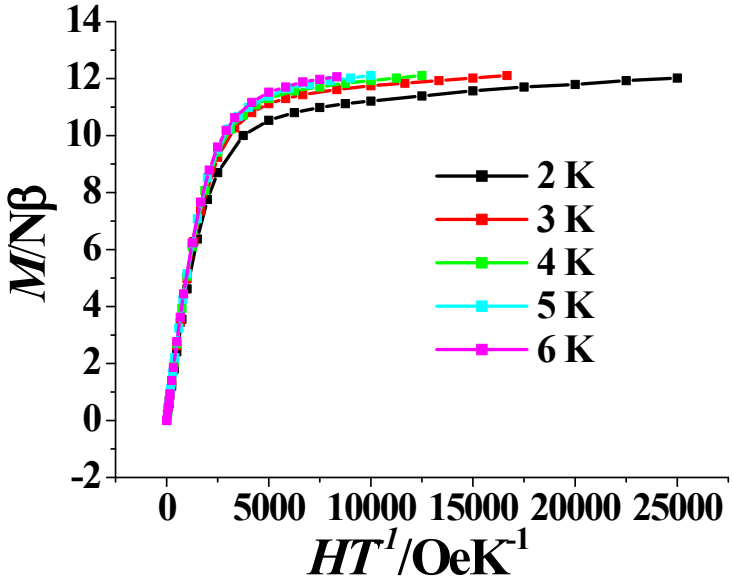

Fig. S7. *M* versus *H*/*T* plots at 2-6 K of **1**.

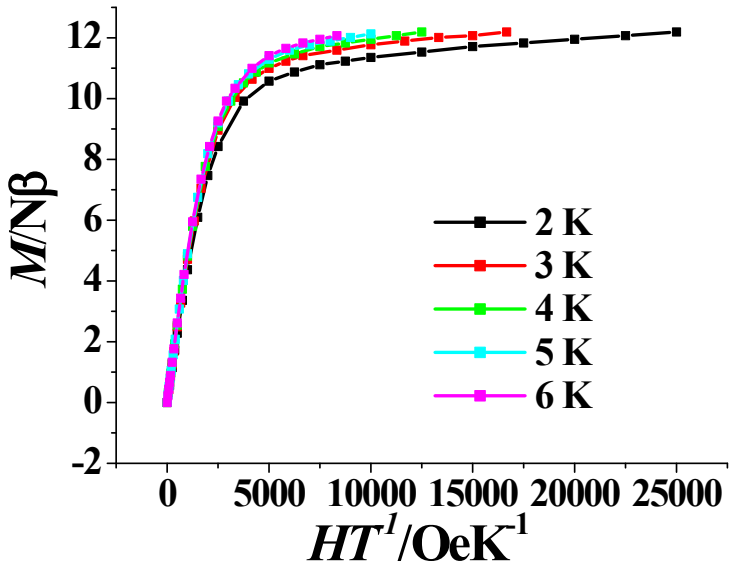

Fig. S8. *M* versus *H*/*T* plots at 2-6 K of **2**.

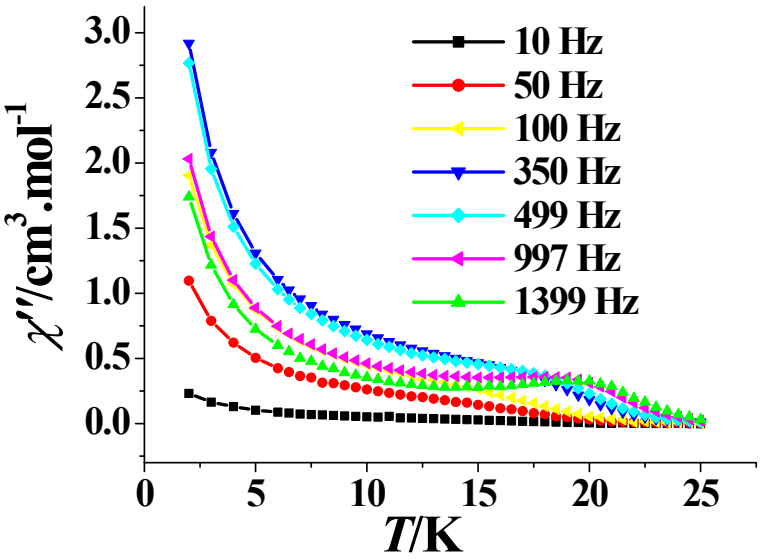

Fig. S9. Temperature dependence of χ'' for **1** under zero dc field.

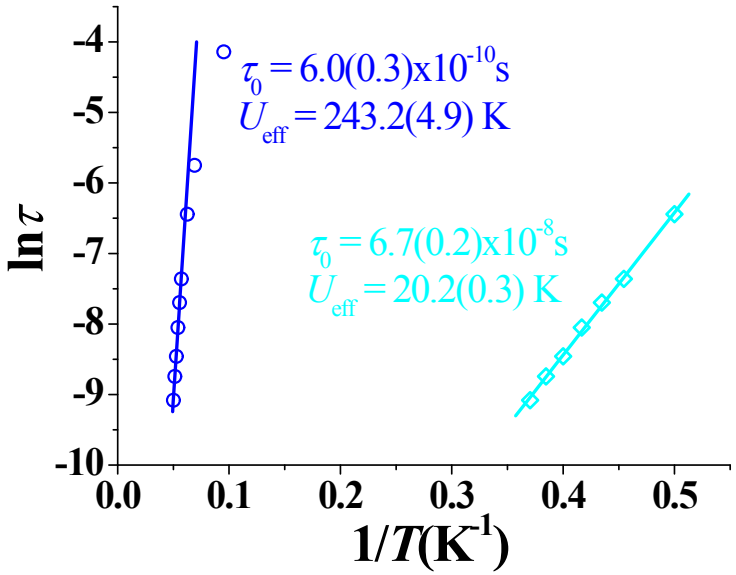

Fig. S10. Plot of ln(τ) versus 1/T for **1** (H_{dc} = 1500 Oe), the solid lines represent the best fitting with the Arrhenius law.

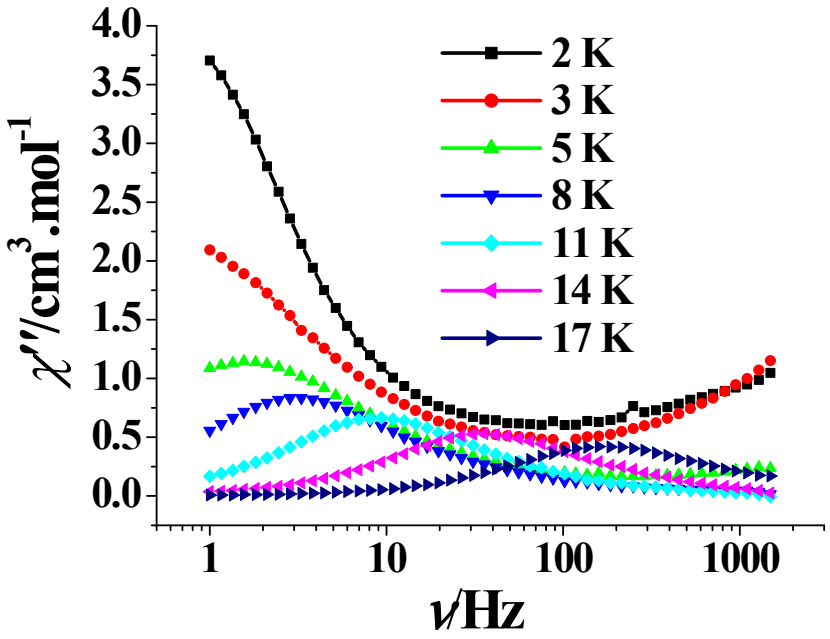

Fig. S11. Frequency dependence of χ'' for **1** under 1500 Oe dc field.

Table S5. Linear combination of two modified Debye model fitting parameters from 2 K to 17 K of **1** under 1500 Oe dc field.

T(K)	χ_2(cm^3.mol^{-1})	χ_1(cm^3.mol^{-1})	χ_0(cm^3.mol^{-1})	τ_1(s)	α_1	τ_2(s)	α_2
2	15.69826	10.0573	0.09782	0.25209	0.150757	0.00003	0.53864
3	13.50628	8.04205	0.59724	0.28748	0.32728	0.00002	0.37736
5	8.07234	6.68125	3.30738	0.10073	0.24662	0.00001	0.41086
8	5.19995	3.54216	3.03447	0.01604	0.44042	0.05292	0.08083
11	3.79315	3.54796	2.25409	0.01865	0.03747	0.00428	0.17766
14	2.98824	1.48366	1.75786	0.02027	0.11029	0.00509	0.15643
17	2.45627	1.9286	1.46514	0.00046	0.11788	0.00126	0.00006

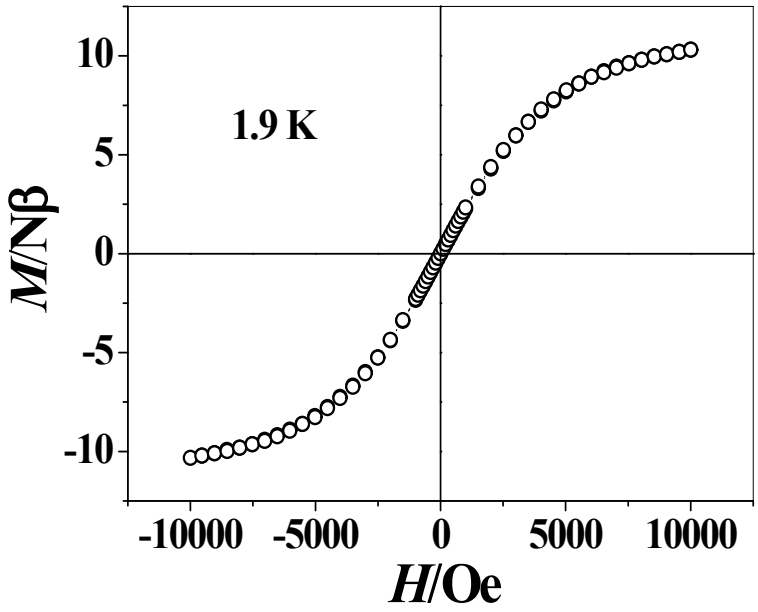

Fig. S12. Hysteresis loop for **1** at 1.9 K.

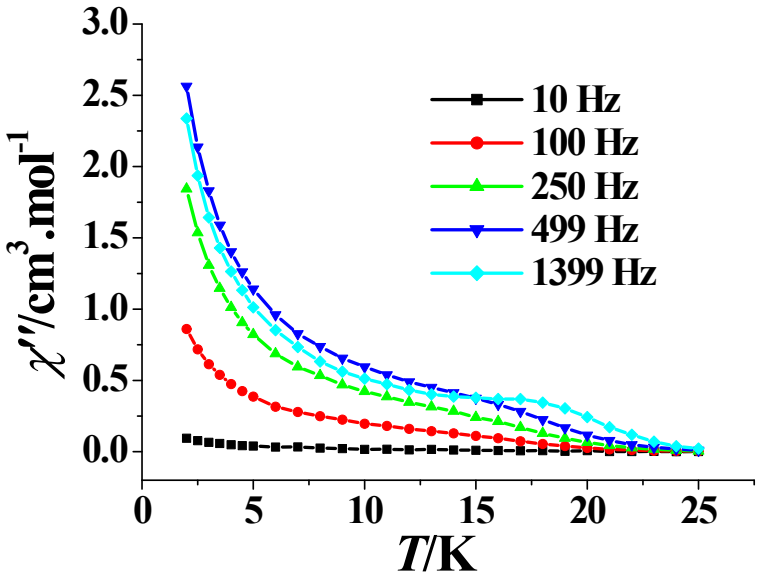

Fig. S13. Temperature dependence of χ'' for **2** under zero dc field.

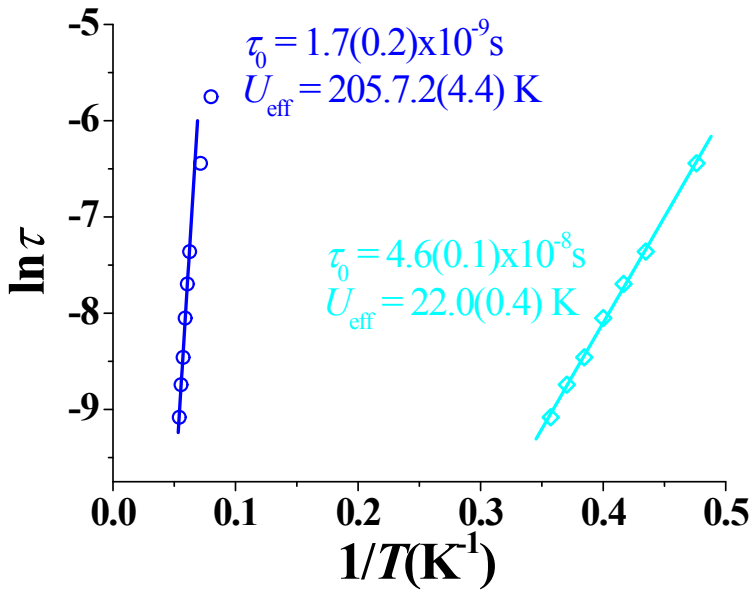

Fig. S14. Plot of ln(τ) versus 1/T for **2** (H_{dc} = 1500 Oe), the solid lines represent the best fitting with the Arrhenius law.

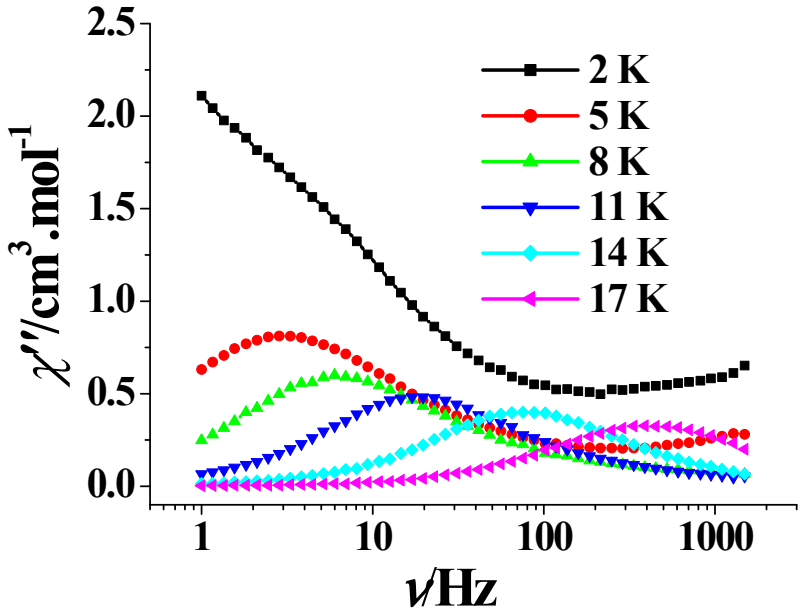

Fig. S15. Frequency dependence of χ'' for **2** under 1500 Oe dc field.

Table S6. Linear combination of two modified Debye model fitting parameters from 2 K to 17 K of **2** under 1500 Oe dc field.

T(K)	χ_2(cm^3.mol^{-1})	χ_1(cm^3.mol^{-1})	χ_0(cm^3.mol^{-1})	τ_1(s)	α_1	τ_2(s)	α_2
2	13.44281	11.85827	2.10398	0.28773	0.47896	0.00006	0.22159
5	5.6251	3.5898	1.16452	0.05286	0.26035	7.3061E-6	0.4617
8	3.62035	3.22313	1.87454	0.02564	0.13496	0.00119	0.5608
11	2.65751	1.56995	1.31141	0.00004	0.57986	0.00843	0.08645
14	2.08701	1.53578	1.15377	0.00107	0.12284	0.00265	0.00568
17	1.73009	1.10962	0.95919	0.00016	0.00003	0.00047	0.06977

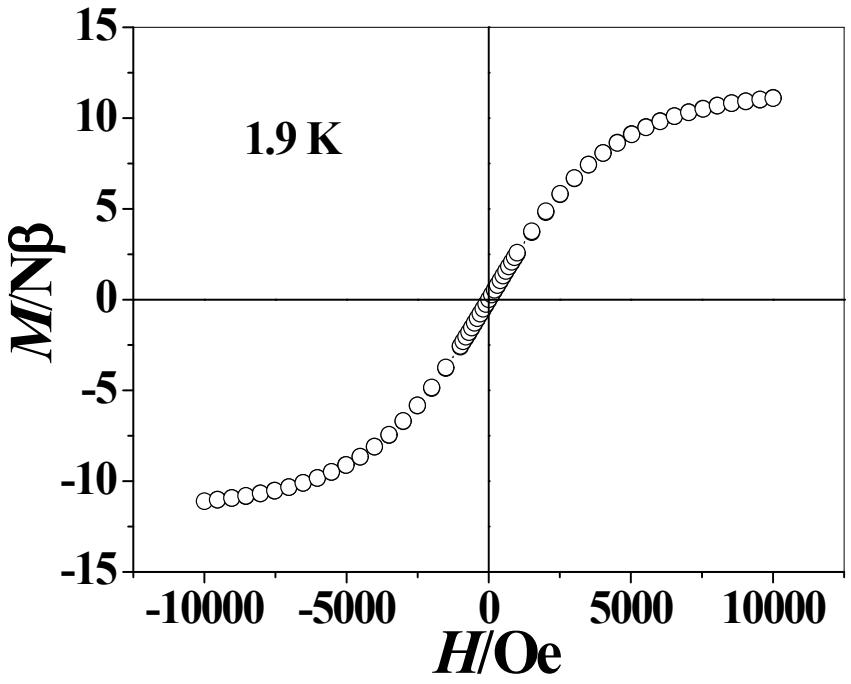

Fig. S16. Hysteresis loop for **2** at 1.9 K.

Computational details

Each binuclear complexes **1** and **2** has two types of Dy^{III} fragments indicated as **1**(**Dy1**), **1**(**Dy2**), **2**(**Dy1**) and **2**(**Dy2**). Complete-active-space self-consistent field (CASSCF) calculations on individual Dy^{III} fragments (see Figure S13 for the calculated structures of complexes **1** and **2**) for compounds **1** and **2** on the basis of single-crystal X-ray determined geometry have been carried out with MOLCAS 8.2[S1] program package. Each individual Dy^{III} fragment in **1** and **2** was calculated keeping the experimentally determined structure of the corresponding compound while replacing the neighboring Dy^{III} ion by diamagnetic Lu^{III}.

The basis sets for all atoms are atomic natural orbitals from the MOLCAS ANO-RCC library: ANO-RCC-VTZP for Dy^{III}; VTZ for close N and O; VDZ for distant atoms. The calculations employed the second order Douglas-Kroll-Hess Hamiltonian, where scalar relativistic contractions were taken into account in the basis set and the spin-orbit couplings were handled separately in the restricted active space state interaction (RASSI-SO) procedure. Active electrons in 7 active spaces include all *f* electrons (CAS(9 in 7 for Dy^{III})) in the CASSCF calculation. To exclude all the doubts, we calculated all the roots in the active space. We have mixed the maximum number of spin-free state which was possible with our hardware (all from 21 sextets, 128 from 224 quadruplets, 130 from 490 doublets). SINGLE_ANISO[S2] program was used to obtain the energy levels, $\boldsymbol{g}$ tensors, m_J values, magnetic axes, *et al.,* based on the above CASSCF/RASSI-SO calculations.

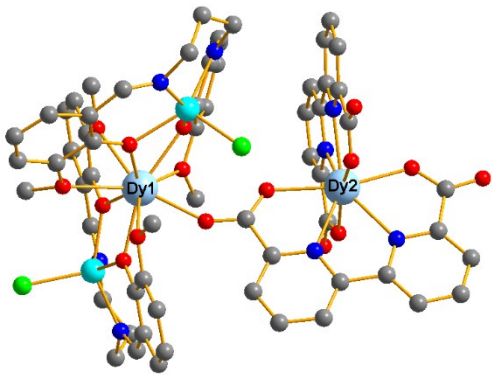

1

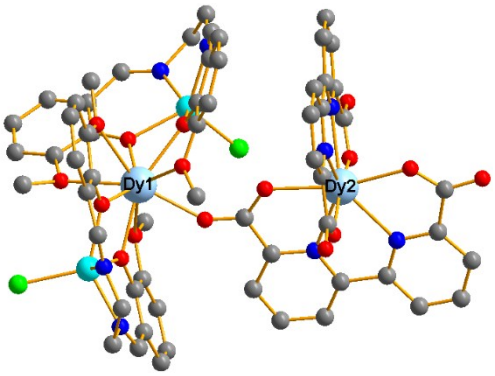

2

Fig. S17. Calculated structures of complexes **1** and **2**; H atoms are omitted.

Table S7. Calculated energy levels (cm^{-1}), ***g*** (g_x, g_y, g_z) tensors and predominant m_J values of the lowest eight Kramers doublets (KDs) of individual Dy^{III} fragments of complexes **1** and **2** using CASSCF/RASSI-SO with MOLCAS 8.2.

KDs	**1(Dy1)**			**1(Dy2)**		
	E/cm^{-1}	***g***	m_J	E/cm^{-1}	***g***	m_J
1	0.0	0.002 0.002 19.783	±15/2	0.0	0.026 0.030 19.671	±15/2
2	156.6	0.057 0.081 18.091	±13/2	136.6	1.164 2.907 16.401	±7/2
3	252.7	0.436 0.999 12.643	±11/2	184.4	0.209 3.434 14.276	±13/2
4	302.6	1.114 4.351 14.420	±7/2	262.6	0.859 2.201 14.697	±9/2
5	320.7	8.424 4.969 1.215	±3/2	347.2	4.893 3.954 2.786	±11/2

6	365.3	0.603 1.853 15.223	±9/2	380.5	1.516 2.838 15.073	±5/2
7	424.4	1.285 2.136 14.172	±1/2	470.0	1.852 2.837 12.702	±3/2
8	591.6	0.095 0.208 18.856	±5/2	555.8	0.596 1.273 16.556	±1/2
KDs	**2(Dy1)**			**2(Dy2)**		
	E/cm^{-1}	$\boldsymbol{g}$	m_J	E/cm^{-1}	$\boldsymbol{g}$	m_J
1	0.0	0.003 0.004 19.778	±15/2	0.0	0.023 0.025 19.713	±15/2
2	151.9	0.075 0.103 18.085	±13/2	165.9	1.071 4.654 14.498	±9/2
3	255.8	0.271 0.707 12.928	±11/2	204.4	0.341 5.437 12.327	±13/2
4	289.2	0.164 1.040 17.731	±9/2	298.7	2.328 3.837 14.720	±7/2
5	332.2	3.962 5.554 9.060	±5/2	376.9	3.207 4.768 7.654	±11/2
6	363.1	0.354 0.551 15.695	±7/2	433.0	0.506 0.969 17.853	±1/2
7	434.2	1.248 2.255 14.233	±1/2	508.9	1.330 2.064 13.482	±5/2
8	606.0	0.097 0.222 18.854	±3/2	611.7	0.301 0.563 17.067	±3/2

Table S8. Wave functions with definite projection of the total moment | m_J > for the lowest two KDs of individual Dy^{III} fragments for complexes **1** and **2** using CASSCF/RASSI-SO with MOLCAS 8.2.

	E/cm^{-1}	wave functions
1(**Dy1**)	0.0	99%|±15/2>
	156.6	54%|±13/2>+16%|±11/2>+13%|±9/2>+14%|±5/2>
1(**Dy2**)	0.0	97%|±15/2>
	136.6	16%|±13/2>+10%|±5/2>+21%|±3/2>+46%|±1/2>
2(**Dy1**)	0.0	99%|±15/2>
	151.9	52%|±13/2>+28%|±11/2>+18%|±9/2>
2(**Dy2**)	0.0	98%|±13/2>
	165.9	26%|±13/2>+9%|±5/2>+19%|±3/2>+41%|±1/2>

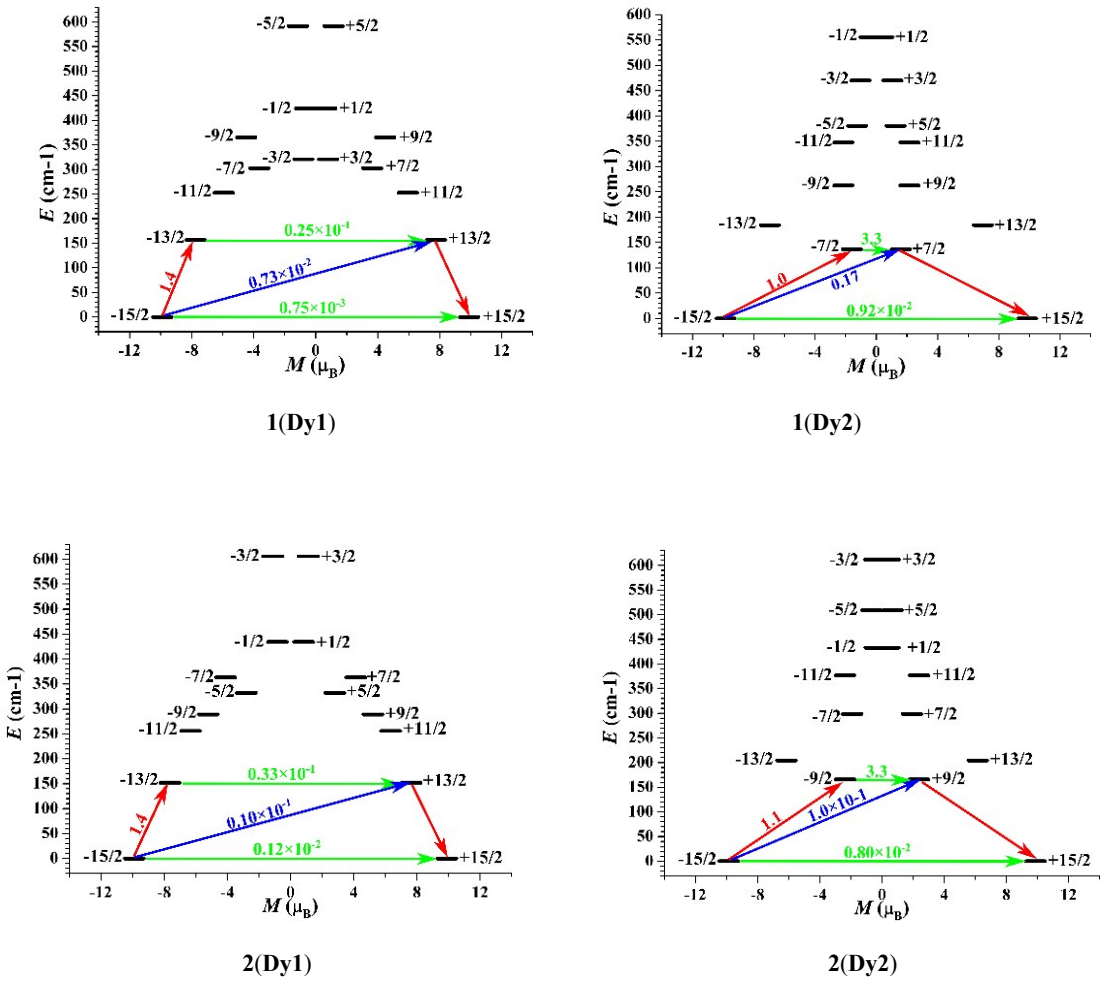

Fig. S18. Magnetization blocking barriers for individual Dy^{III} fragments in complexes **1** and **2**. The thick black lines represent the KDs of the individual Dy^{III} fragments as a function of their magnetic moment along the magnetic axis. The green lines correspond to diagonal matrix element of the transversal magnetic moment; the blue line represent Orbach relaxation processes. The path shown by the red arrows represents the most probable path for magnetic relaxation in the corresponding compounds. The numbers at each arrow stand for the mean absolute value of the corresponding matrix element of transition magnetic moment.

To fit the exchange interactions in complexes **1** and **2**, we took two steps to obtain them. Firstly, we calculated individual Dy^{III} fragments using CASSCF/RASSI-SO to obtain the corresponding magnetic properties. Then, the exchange interaction between the magnetic centers is considered within the Lines model,[S3] while the account of the dipole-dipole magnetic coupling is treated exactly. The Lines model is effective and has been successfully used widely in the research field of *d* and *f*-elements single-molecule magnets.[S4]

For complexes **1** and **2**, there is only one type of *J*.

The Ising exchange Hamiltonian is:

$$H_{exch} = -J S_{Dy1} S_{Dy2} \qquad (1)$$

The total J is the parameter of the total magnetic interaction ($J = J_{diploar} + J_{exchange}$) between magnetic center ions. The $S_{Dy} = 1/2$ is the ground pseudospin on the Dy^{III} site. The dipolar magnetic coupling can be calculated exactly, while the exchange coupling constants were fitted through comparison of the computed and measured magnetic susceptibility using the POLY_ANISO program.[S2]

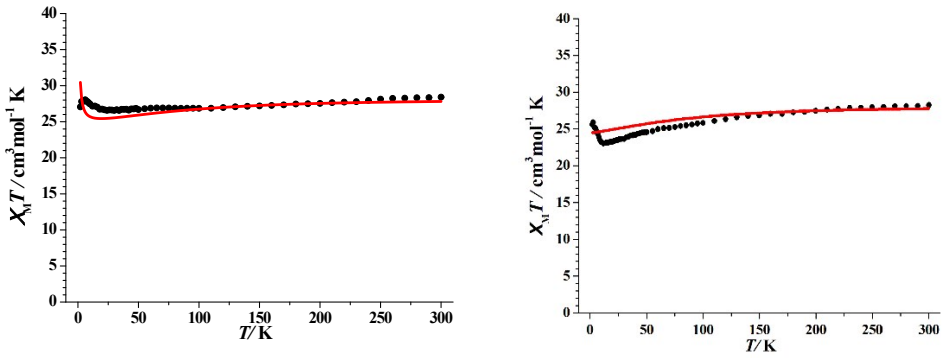

1 **2**

Fig. S19. Calculated (red solid line) and experimental (black circle dot) data of magnetic susceptibilities of **1** and **2**. The intermolecular interactions zJ' of **1** and **2** were fitted to 0.01 and 0.00 cm^{-1}, respectively.

Table S9. Exchange energies E (cm^{-1}), the energy difference between each exchange doublets Δ_t (cm^{-1}) and the main values of the g_z for the lowest two exchange doublets of **1** and **2**.

	1			**2**		
	E	Δ_t	g_z	E	Δ_t	g_z
1	0.00	1.7×10^{-7}	37.483	0.00	4.6×10^{-6}	37.649
2	0.50	2.5×10^{-6}	12.313	0.01	5.1×10^{-5}	11.927

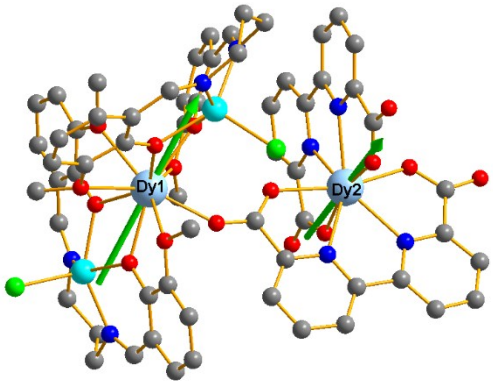

1

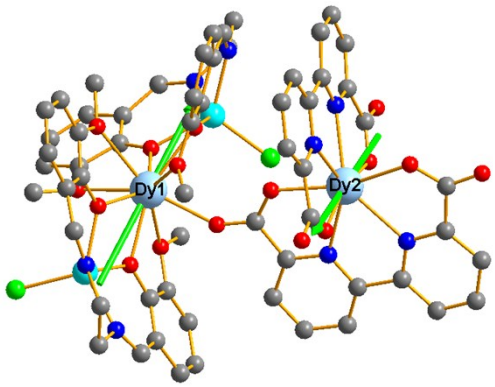

2

Fig. S20. Calculated orientations of the local main magnetic axes in the ground KDs on Dy^{III} ions of complexes **1** and **2**.

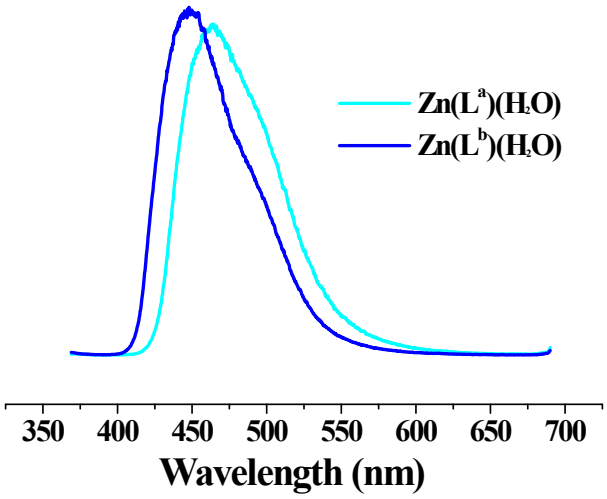

Fig. S21. The solid state emission spectra of $Zn(L^a)(H_2O)$ and $Zn(L^b)(H_2O)$ at room temperature (λ_{ex} = 350 nm).

References:

S1 F. Aquilante, J. Autschbach, R. K. Carlson, L. F. Chibotaru, M. G. Delcey, L. De Vico, I. Fdez. Galván, N. Ferré, L. M. Frutos, L. Gagliardi, M. Garavelli, A. Giussani, C. E. Hoyer, G. Li Manni, H. Lischka, D. Ma, P. Å. Malmqvist, T. Müller, A. Nenov, M. Olivucci, T. B. Pedersen, D. Peng, F. Plasser, B. Pritchard, M. Reiher, I. Rivalta, I. Schapiro, J. Segarra-Martí, M. Stenrup, D. G. Truhlar, L. Ungur, A. Valentini, S. Vancoillie, V. Veryazov, V. P. Vysotskiy, O. Weingart, F. Zapata, R. Lindh, MOLCAS 8: New Capabilities for Multiconfigurational Quantum Chemical Calculations across the Periodic Table, *J. Comput. Chem*., **2016**, *37*, 506.

S2 (a) Chibotaru, L. F.; Ungur, L.; Soncini, A. *Angew. Chem. Int. Ed.*, **2008**, *47*, 4126. (b) Ungur, L.; Van den Heuvel, W.; Chibotaru, L. F. *New J. Chem.*, **2009**, *33*, 1224. (c) Chibotaru, L. F.; Ungur, L.; Aronica, C.; Elmoll, H.; Pilet, G.; Luneau, D. *J. Am. Chem. Soc.*, **2008**, *130*, 12445.

S3 Lines, M. E. *J. Chem. Phys*. **1971**, *55*, 2977.

S4 (a) Mondal, K. C.; Sundt, A.; Lan, Y. H.; Kostakis, G. E.; Waldmann, O.; Ungur, L.; Chibotaru, L. F.; Anson, C. E.; Powell, A. K. *Angew. Chem. Int. Ed*. **2012**, *51*, 7550. (b) Langley, S. K.; Wielechowski, D. P.; Vieru, V.; Chilton, N. F.; Moubaraki, B.; Abrahams, B. F.; Chibotaru, L. F.; Murray, K. S. *Angew. Chem. Int. Ed*. **2013**, *52*, 12014.